# Chapter 12
# Experimental and Numerical Investigation of Internal Gravity Waves Excited by Turbulent Penetrative Convection in Water Around Its Density Maximum

**Stéphane Perrard, Michaël Le Bars, and Patrice Le Gal**

**Abstract** This study is devoted to the experimental and numerical analysis of the excitation of gravity waves by turbulent convection. This situation is representative of many geophysical or astrophysical systems such as the convective bottom layer of the atmosphere that radiates internal waves in the stratosphere, or the interaction between the convective and the radiative zones in stars. In our experiments, we use water as a working fluid as it possesses the remarkable property of having a maximum density at 4 °C. Therefore, when establishing on a water layer a temperature gradient between 0 °C at the bottom and room temperature at the top, a turbulent convective region appears spontaneously under a stably stratified zone. In these conditions, gravity waves are excited by the convective fluid motions penetrating the stratified layer. Although this type of flow, called penetrative convection, has already been described, we present here the first velocity field measurement of wave emission and propagation. We show in particular that an intermediate layer that we call the buffer layer emerges between the convective and the stratified zones. In this buffer layer, the angle of propagation of the waves varies with the altitude since it is slaved to the Brunt–Väisälä frequency which evolves rapidly between the convective and the stratified layer. A minimum angle is reached at the end of the buffer layer. Then we observe that an angle of propagation is selected when the waves travel through the stratified layer. We expect this process of wave selection to take place in natural situations.

S. Perrard (✉)
Laboratoire Matière et Systèmes Complexes, UMR 7057, CNRS/Université Paris Diderot, Bâtiment Condorcet, 10 rue Alice Domon et Léonie Duquet, 75013 Paris, France
e-mail: perrard@clipper.ens.fr

M. Le Bars · P. Le Gal
Institut de Recherche sur les Phénomènes Hors Equilibre, UMR 7342, CNRS/Aix-Marseille Université, 49 rue F. Joliot Curie, 13384 Marseille Cédex 13, France

M. Le Bars
e-mail: lebars@irphe.univ-mrs.fr

## 12.1 Introduction

In most of geo- and astrophysical systems, turbulent convective fluid layers are contiguous with stably stratified zones. Examples include the oceanic upper mixed layer and underlying pycnocline, the atmospheric convective layer and overlying stratosphere, the convective and radiative zones in stars, etc. In classical models of planetary and stellar fluid mechanics, stratified zones are often postulated to be without proper motion. They can nevertheless support oscillatory motions called gravity or internal waves, where the restoring force is due to buoyancy. It has been recognized some 40 years ago in geophysics [3] and more recently in astrophysics [24] that gravity waves can be excited by turbulent convective motions at the interface separating the convective to the stratified fluid domain. This mechanism could be of fundamental importance regarding the transport of momentum and energy through the stratified layer, with important consequences for the system's global organization and evolution. For instance, it has been suggested that in the Earth's atmosphere, the momentum transported by convectively generated gravity waves could drive the quasi-biennial oscillation, i.e. the measured quasi-periodic oscillation of the equatorial zonal wind between easterlies and westerlies in the tropical stratosphere with a mean period of 28 to 29 months [10]. Gravity waves are also known to affect the global momentum budget in the middle and upper atmosphere as well as in the troposphere through wave drag [2]. In stars, convectively generated internal waves constitute an efficient process for angular momentum transport over large distances: they are now seen as an important ingredient in the evolution of rotation within stars [12]. Gravity waves are also invoked as a source of mixing for chemical elements and could help to resolve the enigma of the Lithium dip, forming a coherent picture of mixing in all main sequence stars [21].

Despite a significant number of studies, the current treatment of convectively generated gravity waves still presents major weaknesses. Indeed, the precise mechanism for the generation of such waves, since their typical amplitude as well as their time and space frequency spectra still remain largely unknown. This is mostly due to the difficulties encountered in rigorously describing, in theoretical and numerical models, the transition layer between the convective and the stratified zones, and to simultaneously address a very large range of time and length scales. Two types of approaches can be imagined from a theoretical or a numerical point of view. The first consists in describing the whole system with a single set of equations and methods; but this remains up to now out of reach of theoretical models and of precise numerical simulations (see however the very interesting works in 2D in [18] and [19], and the most recent simulations in 3D by [4], but with a moderate resolution). The second, more widely applied, is to describe separately the convective and stratified zones, which allows one to solve each of them with relevant methods and scales but necessitates that one follows the location of the interface and imposes ad hoc interface conditions that control part of the physical mechanisms. For instance, when considering a fixed interface, coupling is only induced by stresses at the boundary, and the possible effects of interface deformations by overshooting plumes are neglected [21]. In this context, an experimental approach based on relatively simple

laboratory arrangements using water as a working fluid is of great interest, since it allows one to get a global picture of this complex system including all of its interactions and nonlinearities.

Internal waves correspond to periodic density fluctuations in time and space in a stably stratified layer, i.e. where the density decreases with the altitude. In the case of a temperature stratification the Rayleigh number is negative and convective motions will never appear. On the other hand, a small displacement of a fluid particle induces a buoyancy force due to the local difference of density. Writing the classical set of equations for fluid mechanics with a perfect fluid in the Boussinesq approximation and looking for plane wave solutions, the dispersion relation for internal waves can be deduced analytically:

$$\omega^2 = N^2 \sin^2 \theta \qquad (12.1)$$

where $\omega$ is the frequency of the waves, and $\theta$ the angle between the wave vector and the vertical axis. Note that the wavelength does not appear explicitly in this dispersion relation. $N$ is the Brunt–Väisälä frequency given by

$$N(z) = \frac{1}{2\pi} \sqrt{g\alpha(T)\frac{dT}{dz}} \qquad (12.2)$$

where $\alpha(T)$ corresponds to the thermal dilatation coefficient and $g$ to the acceleration of gravity. In the case of a constant temperature gradient and no variation of $\alpha$ with temperature (for instance far from the maximum density of water), the Brunt–Väisälä frequency $N$ remains constant.

Several experimental studies published in the 1960s and 1970s and mostly dedicated to geophysical applications, focus on this internal waves generation by convective motions. Some of them focus on non-stationary situations where an initially thermally stratified layer of water is suddenly heated from below [6]: a convective mixed zone then forms from the bottom of the tank and progressively invades the whole layer of fluid. Others studies benefit from the unusual property of water that its density has a maximum value near 4 °C. Consequently, in a tank filled with water with a horizontal bottom at about 0 °C and a warmer top at room temperature or more, the density stratification is stable in the higher part of the tank and unstable below the 4 °C isotherm. With sufficient separation between the top and bottom plates, the bottom layer is convectively unstable, whereas the upper layer remains stably stratified, allowing one to study stationary configurations once steady-state heat fluxes are established [23]. As expected, in both transient and stationary experiments, the presence of inertial waves in the stratified zone have been observed, based mostly on local temperature measurements. But such local measurements do not allow one to build a global description of the flows, and in particular the coupling between the stable and the unstable layers is still puzzling. To the best of our knowledge, only one recent study by [16] has reinvestigated these questions using modern techniques of non-intrusive global flow measurements, but only for the non-stationary case. Interesting results regarding the excited spectra of internal waves in space and time and the strong two-way coupling between convection and internal waves have, however, been reported. These results now demand confirmation and

generalization in the stationary configuration, which is the purpose of the present study.

In the seventies, McLaren et al. [13] and later Cerasoli [5] investigated the nature and the energy transfer of internal gravity waves generated by a thermal (i.e. an instantaneous release of a buoyant volume of fluid), using respectively particle tracking method and local conduction measurements complemented by dye line visualization. More recently, Ansong and Sutherland [2] have presented experimental results of the generation of internal gravity waves by a turbulent buoyant plume (i.e. a continuous release of buoyant fluid) impinging upon the interface between a uniform density layer of fluid and a linearly stratified layer (all made of salty water). Using non-intrusive schlieren measurements, they determined the fraction of the energy flux associated with the plume at the neutral buoyancy level that is extracted by the waves, and quantified the maximum vertical displacement amplitude. In this case, the frequency of the waves was found to lie in a narrow range relative to the buoyancy frequency, contrary to the numerical results by Rogers and Glatzmaier [18], who predicted a rather extended range for the frequency of waves emitted from a mixing layer. This point will also be discussed here.

## 12.2 Experimental Setup and Measurement Techniques for Penetrative Convection in Water Around 4 °C

To simplify the fluid motions and their measurements, we choose to confine the layer of water between two vertical walls ($x$ and $z$ being respectively the horizontal and vertical coordinates) separated by a short lateral distance equal to 4 cm along the $y$ direction. We have used two different experimental cells that both almost reproduce the Hele–Shaw geometry. The first was built using two Plexiglas plates of dimensions 20 cm × 20 cm in the ($x, z$) plane and thick enough (2 cm) to reduce horizontal outward heat fluxes as the conductivity of Plexiglas is three times lower than the conductivity of water. A second container has been also used. It is taller, allowing a better analysis of the propagation of the internal waves in the stratified layer. It was built by two "vacuumed" glass slabs with a very low thermal conductivity $\lambda_v = 8.4 \times 10^{-2}$ W/K/m, i.e. a hundred times smaller than water conductivity. The $x$ and $z$ dimensions of these windows are 18 cm × 35 cm. The two other lateral vertical walls of both containers were made in Plexiglas with an additional layer of polystyrene foam of thickness 6 cm. The experimental containers were closed by bottom ($z = 0$) and top ($z = 35$ cm or 20 cm) copper plates whose temperatures were regulated by two thermal baths with an accuracy of 0.01 °C. We have checked by visual inspection that as desired, mainly two-dimensional fluid motions take place in the water layers, greatly simplifying the measurements of the velocity field. This narrow geometry also allows us to determine the free position of the separation zone between the convective and the stratified layer which depends on the heat transport. To avoid long thermal transients, we have used the double-bucket technique [17] to prepare a temperature stratified layer of water above a homogeneous layer at 4 °C.

**Fig. 12.1** Schematic representation of our experiment. The non-monotonic water density profile allows us to observe two different layers in a stationary state. The lower one is a turbulent convective layer, whereas the upper layer is stratified where internal waves can propagate
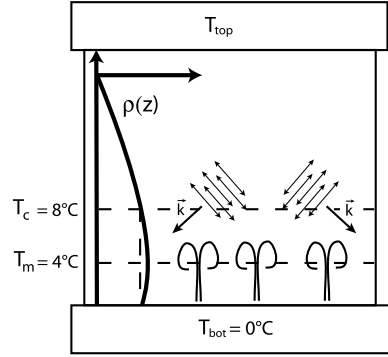


The bottom copper plate temperature is then regulated at $T_{bot} = 0$ °C and the upper at a temperature $T_{top}$ ranging from 18 °C to 35 °C depending on the experimental run. As the density of water increases with the temperature between $T_{bot} = 0$ °C and $T_m = 4$ °C, natural convective motions appear in the bottom layer. This convective layer grows and finally reaches a steady state where its height does not evolve any more. This position is around $z_m \sim 25$ cm from the bottom, which gives a height of 10 cm for the stable stratification in the case where the tall vacuumed-glass container is used. Figure 12.1 gives a schematic representation of the experimental arrangement and of the physical mechanisms of penetrative convection.

Two kinds of measurements were taken in order to characterize both layers. The simplest used local temperature probes. A set of four temperature-type K sensors were positioned at different heights in the middle part of the experimental cell. Another temperature probe was also used to measure vertical temperature profiles. This direct and simple technique was already used (with platinum probes (Pt 100)) by Townsend [23], who reported the first observation of internal waves in water around 4 °C by measuring the temperature fluctuations in the stratified layer. The typical amplitude of temperature fluctuations is $\delta T \sim 0.01$ K, which corresponds to a relative variation of density of $\delta\rho/\rho \sim 10^{-6}$. Note that this amplitude is hundred times smaller than the fluctuation of density usually observed in experiments on internal waves using salt water. An important consequence of this small density gradient is the impossibility to use the now-popular synthetic schlieren method [20]. This technique is based on the variation of the optical refraction index which is undetectable in our case. Therefore, we use the more sensitive Particle Image Velocimetry method (PIV) [1] to directly measure the velocity field associated to the fluid motions. Small particles with a diameter $d = 30$ μm and a density close to the water density (at the temperatures considered here) are used as tracers. Fortunately, the convective motions are turbulent enough to mix these particles in the whole flow within a few days. A laser beam illuminates these particles on a vertical section of thickness 1 mm and $4500 \times 2500$ resolution images are recorded with a numerical photographic camera. A PIV measurement algorithm [15] is then used to extract the velocity fields from the data. Our analysis was performed using typically $128 \times 32$ boxes of $128 \times 32$ pixels with a distance between the centers of two neighboring vertical boxes of

$\Delta Z = 0.15$ mm and $\Delta X = 0.6$ mm between two horizontal boxes. Finally, the time step between two images is chosen between $\Delta t = 5$ s and 20 s. This technique produces velocity maps of $100 \times 80$ vectors as functions of time. The range of velocity values which can be measured with an accuracy better than 5 % depends on the value of $\Delta X$, $\Delta Z$ and $\Delta t$. Owing to the high variation of the velocity along the vertical direction $z$ in the region between the two layers, the PIV parameters are adapted to each measurement, that is why we have used several different time increments. We have chosen rectangular boxes to increase the accuracy along the horizontal direction and the number of measurement points along the vertical direction. After the extraction of the measured velocity field $V(x, z, t)$, we perform a signal analysis in the three-dimensional Fourier space $(f, k_x, k_z)$ for respectively time, $x$ direction and $z$ direction. To separate the weak wave signals from the background noise, we use the singular property of internal waves to propagate in a direction making an angle $\theta$ relative to the vertical direction independent of the wavelength. There are four directions of propagation for each Fourier component $(f, k_x, k_z)$ of the velocity field $V(\mathbf{r}, t)$, making the traditional St. Andrew's cross whose branches are perpendicular to the wave vectors. In our case, as we will see, internal waves may contain a wide range of frequencies, and we need to separate both the Fourier components in time (different values of $f$) and the Fourier components associated to different directions of propagation given by the sign of $k_x$ and $k_z$. To perform this analysis, the velocity field has been studied with the help of the Hilbert transform, a useful tool first used on internal wave observations in [14]. This technic uses the central symmetry of the Fourier transform of a real signal, here $V(x, z, t)$. The wave beam of frequency $f$ propagating along the $(k_x, k_z)$ direction is the sum of two symmetrical Fourier components $(f, k_x, k_z)$ and $(-f, -k_x, -k_z)$. In the spatial Fourier domain, the components of waves propagating along two opposite directions are combined in $(k_x, k_z)$ and $(-k_x, -k_z)$. We separate these components by keeping only the positive frequency in the three-dimensional Fourier space. After performing an inverse Fourier transform in time, each quarter of the $(k_x, k_z)$ space corresponds now to the wave propagating along the chosen direction. We can thus filter and keep only one quarter of the $(k_x, k_z)$ plane and perform the inverse Fourier transform in space to obtain the space-time velocity field $V(x, z, t)$ associated to one of the four beams of the St. Andrew's cross. Additional band-pass filtering in time and space has been also occasionally performed and will be mentioned when used.

## 12.3 Turbulent Penetrative Convection

### 12.3.1 Classical Rayleigh Bénard Convection Between Two Horizontal Plates

A layer of liquid subjected to a negative vertical gradient of temperature between a bottom and a top solid plate is set into motion if the buoyancy force due to the thermal dilatation of the fluid is large enough to compensate for the diffusion of

both temperature and momentum. The associated nondimensional number, called the Rayleigh number, measures the ratio of these destabilizing to stabilizing effects:

$$Ra = \frac{g\alpha \Delta T H^3}{\kappa \nu}, \tag{12.3}$$

where $\alpha$ is the thermal dilatation coefficient, $\Delta T$ the temperature difference between the top and the bottom of the layer, $H$ the height of the fluid layer, and $\kappa$ and $\nu$ respectively the thermal diffusion coefficient and kinematic viscosity. We can note that this Rayleigh number is negative if the temperature gradient has the opposite sign of $\alpha$. For solid boundary conditions, the critical Rayleigh number value is $Ra_c = 1708$ and 1101 for mixed solid/fluid boundary conditions. Far from this threshold, turbulent convection invades the whole fluid layer except for two thin thermal boundary layers of thickness $\delta_c$, confined close to the solid top and bottom plates. The mean temperature in the turbulent bulk is constant equal to $T_m = T_{bot} + \Delta T/2$, in contrast with the temperature in the two boundary layers, which varies linearly with the altitude. $\delta_c$ corresponds to the thickness of these boundary layers for which the local Rayleigh number is equal to the critical value calculated with $\Delta T/2$, i.e.,

$$Ra(\delta_c) = Ra_c, \tag{12.4}$$

where $Ra_c = 1101$. This characteristic length was first introduced by Malkus [11], and the picture of two thin boundary layers of thickness $\delta_c$ separated by a homogeneous bulk at a temperature $T_m$ is now the classical image associated with turbulent Rayleigh–Bénard convection for Rayleigh numbers higher than $10^6$.

### 12.3.2 Penetrative Convection in Water Around 4 °C

For water, the sign of $\alpha$ changes at 4 °C. Thus the lower layer where $0\,°C < T < T_{max} = 4\,°C$ can be unstable if thick enough ($Ra > Ra_c$) contrary to the upper stratified zone corresponding to $T > 4\,°C$ which will be always stable ($Ra < 0$). Using the physical parameters of water, we estimate the value for the Rayleigh number to be around $Ra = 10^7$ for a convective layer of height $H = 15$ cm. This large value for the Rayleigh number justifies to use the approach of Malkus [11] to evaluate the thickness of the bottom diffusive thermal boundary layer in our penetrative convection experiment:

$$\delta_c = \left( \frac{Ra_c \kappa \nu}{g} \frac{\rho_0}{\Delta \rho} \right)^{1/3}, \tag{12.5}$$

where $\Delta \rho / \rho_0$ corresponds to the relative variation of water density between $T_{bot} = 0\,°C$ and $T_{max} = 4\,°C$. As can be seen, $\delta_c$ depends only on the physical properties of water and is equal here to $\delta_c = 0.6$ cm. This value is confirmed by measuring the vertical temperature profile at the bottom of the convective layer, for several values of the temperature at the top ($T_{top} = 8, 15, 20, 35\,°C$), and for both, the Plexiglas and the vacuumed glass tanks ($H = 20$ mm and $H = 35$ mm, respectively).
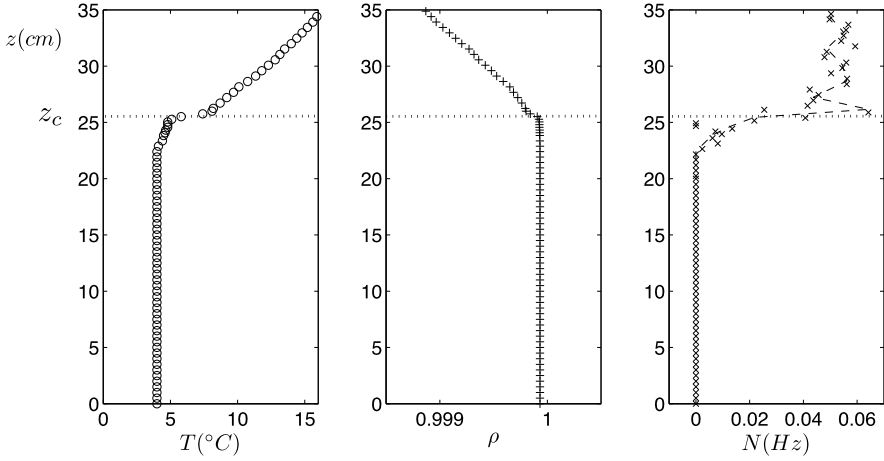
**Fig. 12.2** (**a**) Vertical temperature profile showing the constant temperature in the turbulent convective layer ($0 < z < 23$ cm). (**b**) Vertical density profile calculated from the temperature profile. (**c**) Vertical Brunt–Väisälä frequency $N(z)$. The *dotted line* represents the mean position $z_m$ of the $T_c = 8$ °C isotherm

As presented in Fig. 12.2(a), we measure in the whole convective layer a constant mean temperature $T_m$ equal to $T_{max} = 4$ °C with a typical variation of 0.1 °C. This layer corresponds to a well-mixed zone of water. Close to the density maximum at $T_{max} = 4$ °C, $\rho(T)$ is a symmetric function of $T - T_{max}$, so a fluid particle at 0 °C will have a density equal to one at 8 °C and thus, even in the limit of adiabatic motion, cannot penetrate beyond the 8 °C isotherm. The vertical density profile has been computed using our temperature measurements and the physical properties of water. It is shown in Fig. 12.2(b). The well-mixed layer extends from $z = \delta_c \sim$ 0.6 cm to $z = 23$ cm. For $z > 25$ cm, the density gradient is almost constant, which gives a constant value of $N = 0.05 \pm 0.01$ Hz (see Fig. 12.2(c)). In this region, we expect the propagation of waves to be along straight lines forming different angles $\theta$ with the vertical axis depending on the wave frequency. The vertical position of the limit between the convective and the stratified layers can be determined using the heat flux $Q_d$ through the lower diffusive boundary layer. As the system reaches a stationary state, there is a thermal equilibrium between each layer, and the vertical heat flux $Q(z)$ has to be conserved for all value of $z$. We define this limit by the position $z_c$ of the $T_c = 8$ °C isotherm. In the following, $z_c$ is measured to be around 25 cm. The heat flux verifies the implicit equation

$$Q_d = Q_s, \tag{12.6}$$

where $Q_s$ is the thermal diffusive flux through a stratified layer of thickness $z_{up} - z_c$ subjected to a difference in temperature of $\Delta T = T_{up} - T_c$. Using Fourier's law, we can deduce the value for $z_c$:

$$z_c = \delta_c \frac{T_{up} - T_c}{T_m - T_{bot}}, \tag{12.7}$$
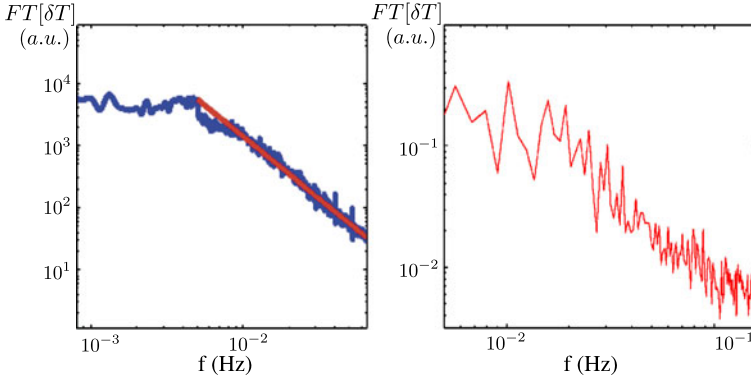
**Fig. 12.3** (**a**) Temporal temperature spectrum in the convective layer. The measurement has been performed by two type K probes. We find a direct energy cascade from small to higher frequencies for $f > f_c \sim 5 \times 10^{-3}$ Hz. (**b**) Temporal temperature spectrum in the stratified layer. Due to their small amplitude, gravity waves are not detected, and the spectrum is typical of a $f^{-1}$ noise spectrum ($f^{-2}$ for the energy spectrum)

where $\delta_c$ corresponds to the thickness of the lower thermal boundary layer (see Eq. (12.5)). As the thickness of the boundary layer $\delta_c$ and the difference of temperature $T_m - T_{\text{bot}}$ are fixed by the maximum density of water at 4 °C, the height of the stratified layer depends only on the temperature imposed at the top of the tank. We remark that between the convective and the stratified zones, we observe an intermediate layer of thickness around two centimeters where the temperature and the density gradients vary with $z$, first slowly, then very rapidly. This zone is in fact delimited by the 4 °C and 8 °C isotherms. This intermediate zone plays an important role in the transmission of both momentum and energy from the convective motions of the internal waves, as we will see below.

Before studying the generation of internal waves and their interaction with convection, we will first describe our natural wave maker, the turbulent convective layer. For this purpose, we perform two point temperature measurements at $z_1 = 5$ cm and $z_2 = 12$ cm (in the container 1) and compute the Fourier transform of $\delta T = T(z_2) - T(z_1)$. This method eliminates the thermal fluctuations of the reference junction. The resulting temperature spectrum ranges from $f = 2 \times 10^{-6}$ Hz to $f = 3$ Hz (see Fig. 12.3(a)). Figure 12.3(b) presents the same spectrum but measured in the stratified layer. As can be seen, no coherent temperature fluctuations are detectable in this zone as the gravity waves amplitude is very small; thus, this spectrum corresponds to thermal noise with a classical power-law proportional to $f^{-2}$. The temperature fluctuations in the convective zone flat part of the spectrum in Fig. 12.3(a) is observed in a large range of frequencies starting from very low frequency (certainly associated to large circulation in the whole container) up to a characteristic frequency $f_c \sim 5 \times 10^{-3}$ Hz. The existence of this characteristic low frequency $f_c$ suggests a production mechanism that forbids the generation of fluctuations at frequencies higher than $f_c$. This effect is in fact also observed in classical turbulent convective systems with top and bottom solid boundaries conditions.

Any temperature fluctuation grows from small perturbations at the solid plate that diffuse in the boundary layer of thickness $\delta_c$ (see Eq. (12.5)) and forms ascendant plumes in the bulk. The rising of one of these convective plumes causes the fluid in the boundary layer to be carried away, and the thin thermal layer has to be rebuilt before another plume could appear. The reconstruction time corresponds to the diffusion time $\tau_c$ for a perturbation to diffuse through this layer. This duration has been evaluated by Howard [8]:

$$\tau_c = \frac{\delta_c{}^2}{\kappa}. \tag{12.8}$$

Using the values corresponding to our experiments ($\kappa$ is equal to $1.36 \times 10^{-7}$ m$^2$/s at 4 °C), we find $\tau_c \sim 250$ s whose inverse has indeed the same order of magnitude as the experimental observed frequency $f_c$ observed on the spectrum (see Fig. 12.3(a)).

As observed in the spectrum of Fig. 12.3(a), an energy cascade takes place for frequencies higher than $f_c$. In the frequency range larger than $f_c$ where the signal-to-noise ratio is larger than 1, we observe an energy cascade on more than 1 decade. The corresponding exponent is equal to $-4 \pm 0.01$ for the energy spectrum. This value is larger (in absolute value) than the typical value around $-2.8$ found in turbulent Rayleigh–Bénard convection [7]. This difference of slope in the spectrum can have two origins. The first reason is the lateral confinement of the flow and the quasi-bidimensional motions of the fluid between the two vertical walls that increases the dissipation at every scale larger than the thickness of the tank. The second reason comes from the main feature of penetrative convection. As there is no longer fixed boundary condition at the top of the convective layer a part of the energy can be transmitted to waves that propagate in the stratified layer. This mechanism induces the radiation of energy by waves that will be damped by viscosity, far from the convective layer. Therefore, the traditional energy cascade is modified by the energy flux which is transmitted to the waves, and can also increases the spectrum exponent. The relative importance of these two processes will be analyzed by the numerical simulations (see Sect. 12.6).

This completes the picture of penetrative convection sketched in Fig. 12.1: a turbulent convective layer with plumes emerging from thermal fluctuations in the bottom diffusive thermal layer at a typical rate around $f_c$. Theses plumes rise through the turbulent convective layer before they excite internal gravity waves when penetrating a buffer zone at the bottom of the stratified layer. One of the possible consequences of this energy release mechanism is that the turbulent spectrum of penetrative convection is steeper than the classical turbulent convection spectrum.

## 12.4 The Buffer Zone Between the Convective and Stratified Layers

After a few days, the convection zone reaches an equilibrium height with two asymmetric boundary layers: the thin lower one and the upper one for which the height is proportional to the imposed temperature difference $T_{\text{up}} - T_c$. By simple visual inspection of tracers, we observe large amplitude motions in the horizontal direction

at a very low frequency in the intermediate buffer zone. At the bottom of the buffer zone, the position of the isotherm 4 °C fluctuates in time when a convective plume goes through the interface. These plumes excite internal waves, their wavelengths being selected by the sizes of the wave makers that generate them. Typically the plumes have a size of $\delta_c$. However, there is also the scale of the whole container as there is always large convective cells, even in the Rayleigh–Bénard turbulent regimes ($R_a > 10^6$) [7]. Thus, we do not expect a sharp length selection, but rather a wave generation on a large range of wavelengths between 0.6 cm and 20 cm.

Using PIV measurement, we observe fluctuations of velocity in space and time. As expected, these fluctuations possess a large range of frequencies around $f_c = 0.02$ Hz but smaller than the Brunt–Väisälä frequency and a large range of wavelengths varying from the size of the box (20 cm) to 1 cm. We observe only waves propagating from the bottom to the top in both horizontal directions ($k_x > 0$ and $k_x < 0$).

The next step in our analysis is to prove that the angle $\theta$ and the associated frequency $f$ of waves follow the dispersion relation given by Eq. (12.1). As these waves are produced by turbulent motions, there is no coherence between successive generated wave packets. Moreover, the duration of propagation through the buffer zone for a wave of typical wavelength of 5 cm will only be a few periods. So the time of coherence has the same order of magnitude as the period of the waves. For such small scale separation, a classical Fourier filtering is not efficient enough to analyze the velocity signal. Thus, we have developed a special data analysis technique, which preserves the signal information localized both in space and time. This technique does not need any supposition on the time of coherence of the generated waves and permits one to determine accurately the mean time-average phase velocity of the waves. To do so, we compute local correlation functions at each point of coordinate $\mathbf{r}$, between $V(\mathbf{r}, t)$ and $V(\mathbf{r} + \delta\mathbf{r}, t + \tau)$:

$$C(\tau, \delta\mathbf{r}) = \frac{1}{T} \int_0^T V(\mathbf{r}, t) V(\mathbf{r} + \delta\mathbf{r}, t + \tau) \, dt. \tag{12.9}$$

For a periodic signal propagating along an arbitrary direction $\mathbf{s}$, the associated correlation function will be periodic in time. The value of the first maximum for a positive time $\tau > 0$ will give the phase shift between $\mathbf{r}$ and $\mathbf{r} + \mathbf{s}$. Along the direction orthogonal to the propagation, the phase shift will vanish. Therefore, we can measure both the phase velocity and its direction as a local function of space and time.

Applying our technique to the measured velocity field in the buffer zone, we can deduce the local mean direction of propagation of internal waves. This angle of mean direction of propagation does not depend on $x$, but as shown in Fig. 12.4, we observe a strong dependence on the altitude $z$. In this buffer zone, the waves do not propagate along a straight line. This result can be linked to the vertical Brunt–Väisälä profile $N(z)$ shown in Fig. 12.2. Indeed, close to the maximum density of water, $N(z)$ scales as

$$N(z) = N_0 \sqrt{\frac{z - z_0}{l_0}} \tag{12.10}$$
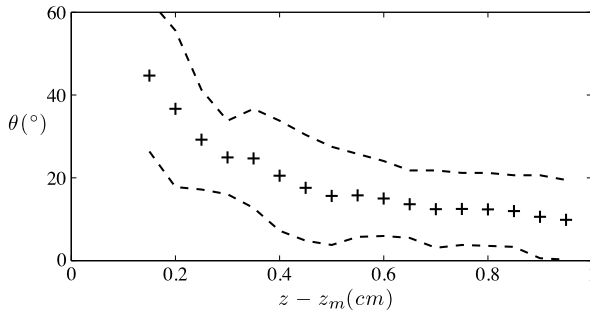
**Fig. 12.4** The direction of propagation $\theta$ of the waves in the buffer zone, obtained by autocorrelation of the velocity fields measured by PIV technique. The *solid line* is the theoretical value of $\theta$, computed with the dispersion relation and the experimental measured values of $N(z)$ plotted on Fig. 12.2. *Dashed lines* represent the bandwidth of $\theta$ of the internal wave packet

where $N_0 = 0.024$ and $l_0 = 1$ cm has been computed using the measured vertical density profile $\rho(z)$ (see Fig. 12.3). The corresponding theoretical curves have been added to Fig. 12.4 (solid lines). It agrees closely with the experimental data with no adjustable parameter. We insist here that this graph represents the mean direction of propagation of wave packets with a large variability around this average value. The dashed line shown on Fig. 12.4 correspond to the uncertainty on $\theta$ due to the large bandwidth of the observed internal waves. Even if we can measure a mean direction of propagation, in the buffer zone there is no narrow selection of the propagation angle of internal waves.

## 12.5 The Stratified Layer

In the buffer layer we have seen that the direction of propagation changes drastically with $z$. As soon as the waves travel out of this layer, the density gradient becomes independent of $z$, and the direction of propagation for each wave will no longer evolve. So in the stratified layer we expect to observe waves propagating straightway in all possible directions with a range of frequencies a priori between 0 and $N$.

With our PIV technique we have measured the velocity field associated with these waves. As before, the spectrum is filtered to keep only the waves propagating along $k_x > 0$ and for all of the frequencies between $0.1N$ and $N$. A PIV snapshot of this field is shown in Fig. 12.5. Contrary to the buffer zone, the wave propagated straightway on a longer distance, more than 10 cm. At this range of propagation, we observe that the waves are damped by viscosity before reaching the top of the tank. It justified a posteriori that there is no significant reflection of waves on the upper copper plate. This feature allows us to evaluate the dissipation along the vertical axis. For this purpose, we compute in the stratified layer the vertical kinetic energy profile $E_c$ given by

$$\langle E_c(z)\rangle = \frac{1}{L}\int_0^L V(z,x)^2\, dx, \qquad (12.11)$$
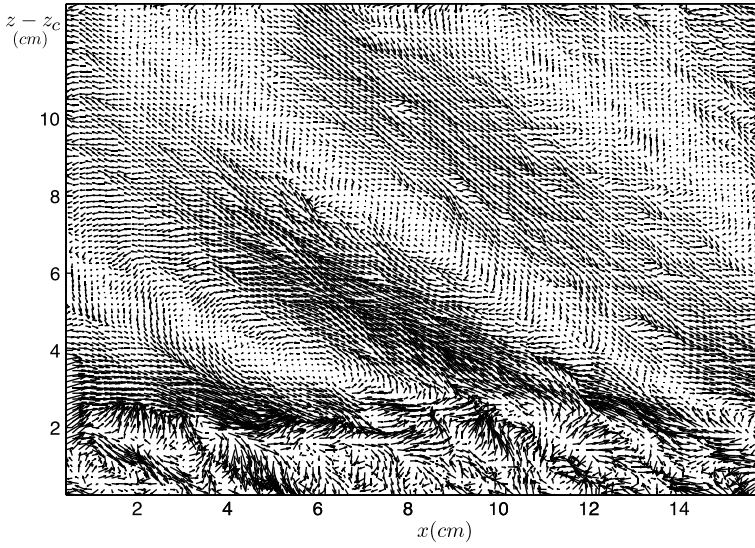
**Fig. 12.5** Instantaneous velocity field in the stratified layer. Only waves propagating toward the right have been kept by our filtering process

**Fig. 12.6** Mean kinetic energy of the gravity waves in the stratified layer as a function of the altitude $z$
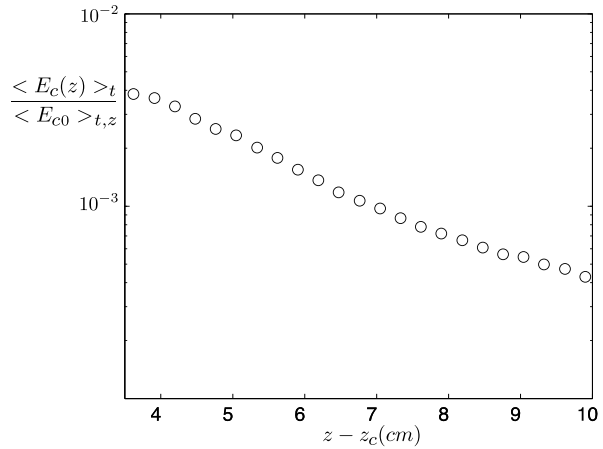


where $L$ corresponds to the horizontal width of the tank. The experimental value of $E_c$ as a function of $z$ is shown in Fig. 12.6. We observe an exponential decay of $E_c$ with the altitude. In the derivation of the internal wave equation it is possible to add the viscous term at the first order [9]. So the viscous damping in amplitude of a wave characterized by its frequency $\omega$ and wavenumber $k$ can be written as

$$A(z) = e^{-\alpha(k)\xi/2}, \quad \text{where } \alpha(k) = \frac{\nu k^3}{\omega\sqrt{(\frac{N}{\omega})^2 - 1}}, \tag{12.12}$$

**Fig. 12.7** The direction of propagation of the waves in the stratified zone, obtained from the velocity fields measured by PIV. In contrast to the buffer zone, here a selection of frequencies and angles is observed. The *dashed lines* represent the bandwidth of $\theta$ of the internal wave packet
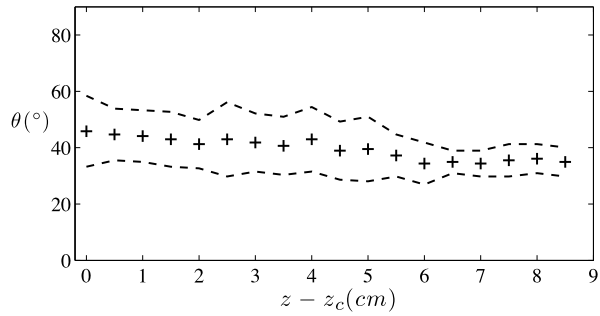
and where $\xi$ corresponds to the coordinate orthogonal to the wave vector. This relation has been verified experimentally [14]. We find an experimental value of $\alpha = 0.21$ cm$^{-1}$, which corresponds to a typical damping length of 3 cm along the vertical axis, which is smaller than the height of the stratified layer. The ratio between the incoming energy from the convective layer and the outgoing energy to the stratified layer being about 20 [23], we can construct an effective damping length for the buffer zone. This length is five times smaller than the one measured in the stratified layer attesting to the fact that the buffer layer avoids the propagation of energy upward.

As we see in Fig. 12.5, the internal waves seem to propagate along a selected direction. To accurately measure the angle of propagation $\theta$, we use the algorithm developed previously for the buffer zone analysis (see Sect. 12.4). We observe in Fig. 12.7 that a narrow range of $\theta$, between 30° and 50°, is selected. This range corresponds to a frequency between $0.4N$ and $0.8N$. For this stratified layer, the dispersion around the mean value is smaller than for the buffer zone. This selection of angle in a stratified layer has also been observed in previous experiments, where internal waves were generated by a turbulent layer [6] or by a single plume [2]. These last authors note, in particular, that an angle of 30° corresponds to the maximum of energy transport by the waves and an angle of 45° to the maximum of momentum transport.

In a closely related study, Taylor and Sarkar [22] suggest a viscous damping mechanism occurring during wave propagation to explain the progressive selection process. Although our study shows an intense damping of the waves in the intermediate buffer layer, together with a selection of the propagation angle of these waves when traveling through and exiting this layer, this explanation is still debated, and more work should be dedicated to definitively answer this question.

## 12.6 Numerical Simulation: To Go Further into the Analysis

To complement this experimental study, a two-dimensional numerical simulation has been performed using the commercial software COMSOL Multiphysics, which is based on the finite-element method. Coupled Navier–Stokes and temperature equations are solved in a square tank of height 35 cm and width 20 cm.

Velocity/temperature boundary conditions are respectively no slip/imposed 0 °C temperature at the bottom, slip/imposed 50 °C temperature at the top, and no slip/imposed heat flux on both sides, mimicking the heat loss by conduction through the 3-cm-thick Plexiglas plates in the experimental setup. Chosen physical parameters are typical for water around 4 °C, with a thermal diffusion coefficient $\kappa = 1.3 \times 10^{-7}$ m$^2$/s, a viscosity $\nu = 1.8 \times 10^{-6}$ m$^2$/s, and an equation of state $\rho = 1 - 8.1 \times 10^{-6}(T - 3.98)^2$. The numerical grid is refined near the boundaries and especially near the lower one to correctly resolve the small-scale dynamics of turbulent plumes. Elements are of standard Lagrange $P_2$–$P_3$ type for solving Navier–Stokes equations (i.e., quadratic for the pressure field and cubic for the velocity field) and are quadratic for solving the temperature field. At each time step the system is solved with the sparse direct linear solver PARDISO.[1] The number of degrees of freedom (DoF) used in the simulations is 125,866. The total duration of the simulation corresponds to a 27.8-hour experiment, starting from a fluid at rest with a uniform temperature of 3 °C in the convective zone $z < 25$ cm and a linear temperature profile from 3 °C to 50 °C in the stratified zone $z > 25$ cm.

Figure 12.8 illustrates the typical state of the convective zone once the turbulent convection is established. As described in the above notes on the experiment, the temperature profile is mostly constant in the bulk with a mean value of about 3 °C and with a thin thermal boundary layer at the bottom. Convective flows correspond to small-scale chaotic plumes growing from the lower boundary, superimposed on a large-scale cellular motion. Typical vertical temperature and velocity vertical profiles extracted at $x = 10$ cm are shown in Fig. 12.9.

The profiles of Fig. 12.9 illustrate the main difficulty of this study: temperature fluctuations above the established linear profile and velocity fluctuations associated with the wave field in the stratified zone are 1 to 2 orders of magnitude smaller than temperature and velocity fluctuations associated with convective motions. This makes them difficult to compute and to observe. Nevertheless, a good way to visualize the wave field is to compute the time derivative of the temperature, as shown in Fig. 12.8; we then notice that the amplitude of the wave pattern rapidly decreases from the interface, as noticed in the experiment.

In order to better investigate the temporal characteristics of the flow, we have analyzed by Fourier transform the temperature at two locations, one in the convective zone and one in the stratified zone. Results are shown in Fig. 12.10(a). For comparison, the same spectra for a simulation with the same parameters but where gravity waves propagation has been artificially prevented by setting the velocity field to zero for $z > 25$ cm is shown in Fig. 12.10(b). We clearly recover the results found in the experiment. The convective spectrum is flat up to the typical cut-off frequency corresponding to $\tau_c$ (see Eq. (12.8)). It then decreases rapidly with a typical exponent $-4$. We do not see significant difference between the convective spectra in the presence and absence of gravity wave, which suggests that this relatively high exponent is mostly due to the two-dimensionality of our study. The spectrum associated with gravity waves clearly shows frequency selection between $3 \times 10^{-3}$ Hz
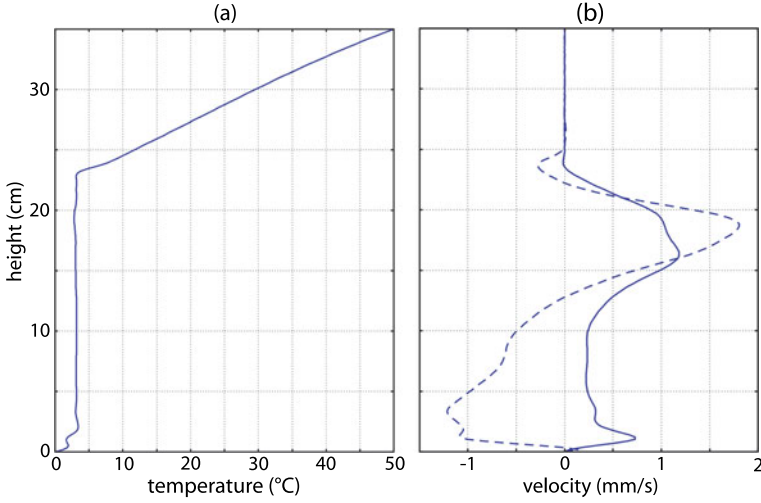
---

[1] www.pardiso-project.org.

**Fig. 12.8** (**a**) Time derivative of the temperature field for locations where $T > 8\,°C$ (i.e. in the stratified zone) obtained at time $t = 27.8$ hours. Also shown is the velocity field (*black arrows*); (**b**) temperature field (in *color*, between $0\,°C$ and $8\,°C$ in order to focus on the convective zone) and velocity field (*black arrows*) obtained at time $t = 27.8$ hours
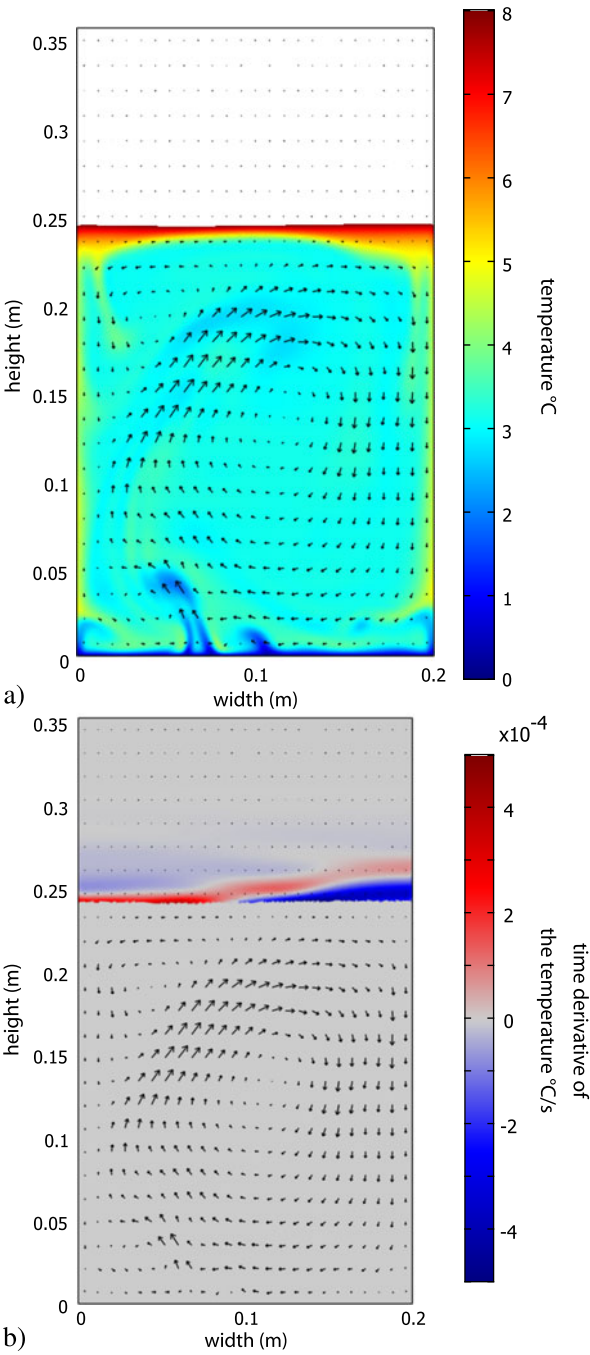
**Fig. 12.9** Vertical profiles for (**a**) the temperature and (**b**) the vertical (*solid*) and horizontal (*dashed*) velocity at time $t = 27.8$ hours in the middle of the tank ($x = 10$ cm)
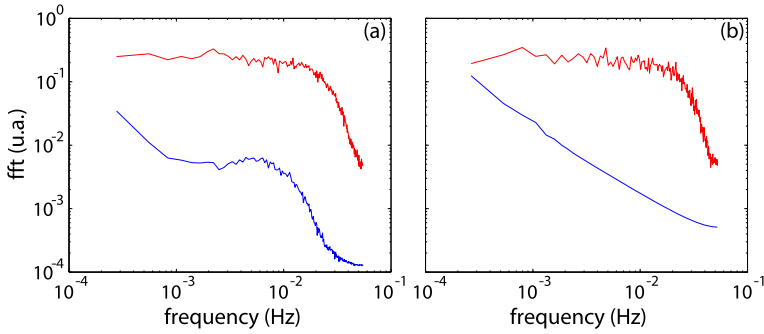


**Fig. 12.10** Temporal temperature spectrum in the convective layer (*upper curve*, signal measured at $x = 17$ cm and $z = 10$ cm) and in the stratified layer (*lower curve*, signal measured at $x = 17$ cm and $z = 28$ cm): (**a**) for the standard simulation and (**b**) for a simulation with the same parameters but where gravity waves propagation has been artificially prevented by setting the velocity field to zero for $z > 25$ cm. Each curve corresponds to the mean value of the Fourier transforms over a sliding window of 1 hour of the signal corrected by a degree 1 polynomial fit (to suppress the long term drift), from time $t = 1.5$ hour to time $t = 27.8$ hours

and $7 \times 10^{-3}$ Hz, corresponding to propagation angles between 25° and 60°, the favorite angle being around 40°. By comparison, the corresponding spectrum in the absence of waves propagation (the waves have been artificially prevented) is typical of an $f^{-2}$ noise spectrum, highlighting the good resolution of the wave field by our method.

## 12.7 Conclusion

In this study, we have used the very peculiar property of water of having a maximum density at a temperature of 4 °C. This property has permitted the experimental investigation of penetrative convection in a stationary regime. Turbulent convection that sets in the lower part of a water layer cooled by its bottom plate at a temperature lower than 4 °C can generate gravity waves in the upper stably stratified layer. These waves are excited by the rising of turbulent plumes impinging the bottom of the stratified layer. Although dealing with the small values of the involved density gradients is a challenging task, this difficulty has been circumvented using a very sensitive PIV technique, which is then combined with a dedicated data analysis. Our experimental study is then completed by a 2D numerical direct simulation. In both experimental and numerical investigations, we recover the known selection of propagation angles of the waves in the stratified layer. We have however identified a third layer squeezed between the convective and the stratified layers that we have called the buffer layer and where the Brunt–Väisälä frequency varies with the altitude. In this zone there is no angle selection and a strong damping in the vertical direction. We expect the different properties of penetrative convection that we studied here to apply in natural situations such as the generation and the propagation of g-waves in star radiative zones or internal waves excitation in the stratosphere or in the oceans.

## References

1. Adrian, R.J.: Particle-imaging techniques for experimental fluid-mechanics. Annu. Rev. Fluid Mech. **23**, 261–304 (1991)
2. Ansong, J.K., Sutherland, B.R.: Internal gravity waves generated by convective plumes. J. Fluid Mech. **648**, 405 (2010)
3. Bretherton, F.P.: On the mean motion induced by internal gravity waves. J. Fluid Mech. **36**, 785–803 (1969)
4. Brun, A.S., Strugarek, A.: Understanding the solar inner magnetism and dynamics. In: Sekii, T., Watanabe, T., Sakurai, T. (eds.) Proceedings of the 3rd Hinode Science Meeting, 1–4 December 2009. ASP Conf. Ser., vol. 454 (2012)
5. Cerasoli, C.P.: Experiments on buoyant-parcel motion and the generation of internal gravity waves. J. Fluid Mech. **86**, 247–271 (1978)
6. Deardorff, J.W., Willis, G.E., Lilly, D.K.: Laboratory investigation of non-steady penetrative convection. J. Fluid Mech. **35**, 7–31 (1969)
7. Heslot, F., Castaing, B., Libchaber, A.: Transitions to turbulence in Helium gas. Phys. Rev. A **36**, 5870–5873 (1987)
8. Howard, L.N.: Convection at high Rayleigh number. In: Proc. 11. Int. Congr. Appl. Mech., pp. 1109–1115 (1964)
9. Hurley, D.G., Keady, G.: The generation of internal waves by vibrating elliptic cylinders. Part 2. Approximate viscous solution. J. Fluid Mech. **351**, 119–138 (1997)
10. Lindzen, R.S., Holton, J.R.: A theory of the quasi-biennial oscillation. J. Atmos. Sci. **25**, 1095–1107 (1968)
11. Malkus, W.V.R.: The heat transport and spectrum of thermal turbulence. Proc. R. Soc. Lond., Ser. A **225**, 196–212 (1954)
12. Mathis, S., Talon, S., Pantillon, F.P., Charbonnel, C., Zahn, J.P.: Wave transport in stellar radiation zone influenced by the Coriolis acceleration. J. Phys. Conf. Ser. **118**(1), 012025 (2008)

13. McLaren, T.I., Pierce, A.D., Fohl, T., Murphy, B.L.: An investigation of internal gravity waves generated by a buoyantly rising fluid in a stratified medium. J. Fluid Mech. **57**, 229–240 (1973)
14. Mercier, M.J., Garnier, N.B., Dauxois, T.: Reflection and diffraction of internal waves analyzed with the Hilbert transform. Phys. Fluids **20**(8), 086601 (2008)
15. Meunier, P., Leweke, T.: Analysis and treatment of errors due to high velocity gradients in particle image velocimetry. Exp. Fluids **35**, 408–421 (2003)
16. Michaelian, M.: The coupling between turbulent, penetrative convection and internal waves. Eur. J. Mech. B, Fluids **21**, 1–28 (2002)
17. Oster, G.: Density gradients. Sci. Am. **213**, 70–76 (1965)
18. Rogers, T.M., Glatzmaier, G.A.: Penetrative convection within the anelastic approximation. Astrophys. J. **620**, 432–441 (2005)
19. Rogers, T.M., MacGregor, K.B.: On the interaction of internal gravity waves with a magnetic field—II. Convective forcing. Mon. Not. R. Astron. Soc. **410**, 946–962 (2011)
20. Sutherland, B.R., Dalziel, S.B., Hughes, G.O., Linden, P.F.: Visualization and measurement of internal waves by synthetic schlieren. Part 1. Vertically oscillating cylinder. J. Fluid Mech. **390**, 93–126 (1999)
21. Talon, S., Charbonnel, C.: Angular momentum transport by internal gravity waves. I—Pop I main sequence stars. Astron. Astrophys. **405**, 1025–1032 (2003)
22. Taylor, J.R., Sarkar, S.: Internal gravity waves generated by a turbulent bottom Ekman layer. J. Fluid Mech. **590**, 331–354 (2007)
23. Townsend, A.A.: Natural convection in water over an ice surface. Q. J. R. Meteorol. Soc. **91**, 243–245 (1965)
24. Zahn, J.P., Talon, S., Matias, J.: Angular momentum transport by internal waves in the solar interior. Astron. Astrophys. **322**, 320–328 (1997)